Time- and space-resolved spectroscopic characterization of laser-induced swine muscle tissue plasma.

J. J. Camacho[1], L. Diaz[2,*], S. Martinez-Ramirez[2], J. O. Caceres[3]

[1]Departamento de Química-Física Aplicada. Facultad de Ciencias. Universidad Autónoma de Madrid. Cantoblanco. 28049-Madrid. Spain

[2]Instituto de Estructura de la Materia, CFMAC, CSIC, Serrano 121. 28006-Madrid, Spain

[3]Departamento de Química Analítica, Facultad de Ciencias Químicas, Universidad Complutense, Cuidad Universitaria, 28040-Madrid, Spain.

[*]Corresponding author: e-mail: luis.diaz@csic.es

Abstract

The spatial-temporal evolution of muscle tissue sample plasma induced by a high-power transversely excited atmospheric (TEA) CO_2 pulsed laser at vacuum conditions (0.1-0.01 Pa) has been investigated using high-resolution optical emission spectroscopy (OES) and imaging methods. The induced plasma shows mainly electronically excited neutral Na, K, C, Mg, H, Ca, N and O atoms, ionized C^+, C^{2+}, C^{3+}, Mg^+, Mg^{2+}, N^+, N^{2+}, Ca^+, O^+ and O^{2+} species and molecular band systems of $CN(B^2\Sigma^+ - X^2\Sigma^+)$, $C_2(d^3\Pi_g - a^3\Pi_u)$, $CH(B^2\Sigma^- - X^2\Pi$; $A^2\Delta - X^2\Pi)$, $NH(A^3\Pi - X^3\Sigma^-)$, $OH(A^2\Sigma^+ - X^2 \Sigma^+)$, and $CaOH(B^2\Sigma^+ - X^2\Sigma^+$; $A^2\Pi - X^2\Sigma^+)$. Time-resolved two-dimensional emission spectroscopy is used to study the expanded distribution of different species ejected during ablation. Spatial and temporal variations of different atoms and ionic excited species are reported. Plasma parameters such as electron density and temperature were measured from the spatio-temporal analysis of different species. Average velocities of some plasma species were estimated.

1. Introduction

Laser-produced plasmas (LPPs) are formed by focusing a high-power laser onto a sample. The induced plasma expands quickly and their characteristic parameters change with distance and time.

Because of the transient characteristics of the plasma-plume, optical emission spectroscopy (OES) technique with time and space resolution is especially suitable to obtain information about the behavior of the produced species as well as to study the dynamics of the plasma expansion. Although OES gives only partial information about the plasma particles, this diagnostic technique helped us to draw a picture of the plasma in terms of the emitting chemical species, to evaluate their possible mechanisms of excitation and formation and to study the role of gas-phase reactions in the plasma expansion process. Measurements of the plasma density and temperatures are important to obtain information about plasma expansion dynamics. The plasma characteristics vary considerably with distance from the target surface both in the plume expansion direction (axial) and orthogonal to plume expansion directions (radial), as well as with time following the beginning of plasma-plume formation.

Currently there are numerous applications for LPPs in a wide variety of fields, including laser-induced breakdown spectroscopy (LIBS) [1-4], pulsed-laser deposition (PLD) [5,6], distinguishing of explosives [7-13], environmental science [14-16], production of classical and novel materials [17-18], cultural heritage monitoring [19] or space exploration [20-22]. Beyond traditional applications of LIBS, where inorganic materials are mainly studied for analytical purposes, recent progresses in LIBS lead to analysis of organic and biological samples for detection of chemical and biological warfare agent materials [23-28], animal tissues studies [29-37], identification of bacteria [38-48], etc. Several reviews have been published that discuss various aspects of LIBS biomedical application [1-4, 49,50]. Recent developments of LIBS for biological material analysis potentially provide fast sensor systems for pathogen biological agent detection and analysis.

Because of highly transient nature of the LPP, the plasma-plume properties should be optimized for each application and the plasma diagnostics play a key role in this regard. In particular, the estimation of the post-mortem interval (PMI) by LIBS using swine muscle has

created interest due to its cost-effective analysis [50]. It can be expected that the determination of PMI can be improved by using high resolution OES.

This article reports the first spatial and temporal study the dynamics of the ablated swine tissue plasma-plume produced in vacuum. The plasma was generated by focusing a transversely excited atmospheric (TEA) CO_2 pulsed laser on the target placed in a vacuum chamber. We have studied the dynamics of laser ablated plasma expanding into vacuum using simultaneous imaging and spectroscopic techniques. Time-resolved spectra, that were also spatially resolved in one dimension along the axis of plasma expansion, were obtained using a time gated intensified charge-coupled device (ICCD). We discuss the dynamics of the plume expansion and formation of different atomic and ionic species for different positions and delay times with respect to the beginning of the laser pulse. Analysis of the image spectra provides useful plasma parameters such as velocities of different plasma species, electron density and temperature.

2. Experimental procedures

The schematic of the experimental setup is given in Fig. 1. Pulses from a TEA CO_2 laser (Lumonics K-103) emitting at 10.591 μm are used for producing plasmas on a skeletal muscle sample of a swine [51]. To ensure sample homogeneity, swine tissues were lyophilized and compressed into a pellet. The excitation wavelength was checked with a spectrum analyzer (Optical Eng. Co.). At the sample position, the laser delivered up to 3.16 J at 10.591 μm, leading to an estimated power of 49.5 MW, power density or intensity of 6.31 GW×cm^{-2}, fluence of 410 J×cm^{-2}, photon flux of 3.1×10^{29} photon×cm^{-2}×s^{-1}, electric field of 1.54 MV×cm^{-1} and radiation pressure of 421 kPa [51,52]. The primary laser beam (divergence of 3 mrad) was angularly defined and attenuated by an iris of 17.5 mm diameter before entering into the vacuum chamber. A beam splitter was employed to redirect about 10% of the laser pulse energy on a pyroelectric detector (Luminics 20D) or on a photon drag detector (Rofin Sinar 7415) for energy and temporal shape monitoring and triggering, respectively, through a digital oscilloscope (Tektronic TDS 540). The temporal profile of the laser pulse is 65 ns full width at half maximum (FWHM) followed by a tail lower than

2 μs controlled by changing the gas mixture flowing through the cavity (typically 8:8:84 mixture of CO_2:N_2:He). The laser-pulse energy was varied by using several CaF_2 attenuating plates.

Fig. 1. Close to here.

The target is placed at the centre of a vacuum chamber pumped using a turbomolecular pump, and a vacuum of 0.01 Pa has been achieved in all our experiments. The target was mounted on a rotating holder to diminish the effects produced by crater formation. The laser beam was focused on the target by a NaCl lens of 24 cm focal length being the measured focused-spot area $\approx 7.9 \times 10^{-3}$ cm^2. The laser fluence was calculated as the ratio of the pulse energy (Lumonics 20D pyroelectric detector through a Tektronix TDS digital oscilloscope) and $1/e$ cross-sectional beam area (measured at the target position with a pyroelectric array Delta Development Mark IV). Two spectrometers were used: one with a resolution of $\approx$ 1 nm (portable BWTEK, 25 μm slit, 600 grooves×mm^{-1} grating) and the other with a resolution of $\approx$ 0.02 nm (ISA Jobin Yvon Spex HR320, adjustable width slit, 2400 grooves×mm^{-1} holographic grating). For performing time and space resolved OES, the plasma emission was collected and imaged onto the slit of the high-resolution spectrograph. We have set the origin of axial distance, $z = 0$ mm, as the target surface. In our setup target and focusing lens can be displaced across the beam axis.The intensity response of the detection system was calibrated with a standard halogen lamp (Osram number 4385, 6.6 A, 200 W) [53]. Several hollow-cathode lamps were used for wavelength calibration. A quartz Dove prism was inserted into the optical path for capturing two-dimensional (2D) spectral imaging and rotating the plasma image by 90º, projecting the direction of the plasma expansion (Z-axis) onto the entrance slit. The Dove prism is placed between two crystal lenses with focal distances of 80 mm (L1) and 40 mm (L2). The magnification of the final image formed by the optical system was found to be 1:0.5. The 2D spectral images were recorded by a gateable ICCD (Andor iStar DH-734, 1024 × 1024 pixels, 13 μm pixels). For time-resolved measurements, the ICCD detector is synchronized with the trigger of the laser pulse. The 2D spectral imaging studies were performed

by operating the ICCD in the imaging mode. Each spectrum corresponds to an accumulation of 10 laser pulses.

3. Results and discussions

The interaction of a focused high-power laser with a swine tissue sample leads to the formation of a plasma. This plasma quickly expands freely into a vacuum in a direction perpendicular to the target surface. Fig. 2 shows a typical low-resolution, time-integrate one-dimensional (1D) OES from LPP of muscle tissue sample at a constant distance of 2 mm from the target surface. The spectrum is compared to the atomic/ionic lines of Na, K, Mg, Mg^+, C, C^+, N, N^+, O, and H along with the corresponding relative intensities tabled in NIST Atomic Spectral Database [54].

The assignments of some atomic/ionic lines and some molecular bands are shown. In this experiment, the CO_2 laser delivers 80 J/cm^2 and the exposure time of the image intensifier, typically referred to as the gate width time, 20 μs. Strong C^+, N^+, Na, H, K and O lines and molecular bands of CN ($B^2\Sigma^+ - X^2\Sigma^+$) dominate the spectrum. The medium-weak emission is due to excited species C, C^{2+}, C^{3+}, Mg, Mg^+, Mg^{2+}, N^{2+}, Ca, Ca^+, O^+, Fe, Zn, P and molecular bands of $C_2(d^3\Pi_g - a^3\Pi_u)$, CH($B^2\Sigma^- - X^2\Pi$; $A^2\Delta - X^2\Pi$), NH($A^3\Pi - X^3\Sigma^-$) and OH($A^2\Sigma^+ - X^2\Sigma^+$). Other weak molecular band systems are in evidence including systems from N_2, N_2^+ and CaOH($B^2\Sigma^+ - X^2\Sigma^+$; $A^2\Pi - X^2\Sigma^+$). The relative intensities of the observed atomic/ionic emission lines reasonably agree with tabulated values in NIST. The spectral features clearly show the complexity of the relaxation process.

Fig. 2. Close to here.

In order to get more insight into laser produced swine tissue sample plasma and to obtain an unambiguous assignment of the emission, we have scanned the spectra at high-resolution. For the

spectral identification, the observed LPP spectrum of the swine tissue sample was compared with the spectra obtained in our laboratory in other experiments. As an example, Fig. 3 shows several OES at high resolution obtained in our laboratory from LPP of O_2, air, graphite and graphite in N_2 atmosphere performed at different fluences ranging between 123 J×cm^{-2} and 410 J×cm^{-2}, z=0, delay = 0 μs and a width gate of 0.1 μs for swine sample and 20 μs for the rest [55-58]. The identification of the line at 253 nm was difficult due to the possible spectral overlapping of two lines of C^{3+} and Mg^{2+}.

Fig. 3. Close to here.

In addition, the temporal evolution of the optical emissions was studied to understand the dynamics of the laser-ablated plasmas. The time for the onset of the laser pulse is considered as the origin of the time scale. The spectra have been obtained in the region 243–256 nm, at a delay time ranging from 0 to 5 μs at 0.1 μs intervals and at an observation distance $z = 2$ mm.

Fig. 4 displays the time-resolved LPP (laser fluence 123 J×cm^{-2}) spectra in this spectral region. This region was chosen in order to detect highly ionized carbon, oxygen and magnesium species and atomic carbon lines. During the initial stages after the peak intensity laser pulse ($t_d \leq$ 0.1 μs), emissions from different ionic species (C^{3+}, Mg^{2+}, O^{2+}, C^+, Mg^+ and O^+) dominate the spectrum. After 0.3 μs, the spectrum is dominated by C spectral emission line at 247.9 nm. Spectrum narrowing was observed with increasing delay as the consequence of the decrease of the temperature and electron density. Highly ionized species such as C^{3+}, Mg^{2+}, O^{2+}, and O^+ were detected up to 0.6 μs, C^+ up to 1 μs and C up to 4 μs.

Fig. 4. Close to here

The temporal evolution of spectral atomic and ionic line intensities at a constant distance from the target has been used to build the optical time-of-flight (TOF) profiles shown in Fig. 5. The temporal profile of the laser pulse at 10.591 μm is also shown.

Fig. 5. Close to here

The TOF distributions of C^{3+} (252.426 nm), O^{2+} (245.497 nm), N^+ (249.681 nm), and C^+ (251.174 nm) species were found to consist approximately of one strong intense maximum at 0, 0, 0.1, and 0.1 μs, respectively. This behavior is very similar to other species with the same ionization stage. The emission intensity of C^{3+} decreases faster than the emission intensity of the other ionic lines. The TOF distribution of C (247.856 nm) atoms was found to consist approximately of one weak intense maximum at 0.1 μs and one strong maximum at 0.6 μs. The time duration of different lines of C, C^+, N^+, O^{2+}, and C^{3+} were nearly 4, 1, 0.5, 0.7 and 0.4 μs, respectively. The observed delay between C and C^+ species, with respect to C^{3+} ions TOF maxima, indicates the recombination of C^{3+} with electrons to form those species. All these data show the relative fast recombination of these ionic species.

The LPP spectra of the tissue sample were recorded as a function of the emitted wavelength, delay time and distance from the target. This type of study has been previously reported by different authors [59-69]. In order to study the plasma plume expansion dynamics for different species, we plotted 2D image spectra versus time delay. The 2D spectral imaging technique provides spatially- and spectrally-resolved information about the plasma. However, the intensity profiles are only suitable for average expansion velocity estimation, but they are not enough for an appropriate description of the plasma and of the distribution of species. Relative number densities are necessary for this, so to account for possible differences in the spectroscopic data of the various considered transitions, and, even more important, for different plasma temperatures in the different plasma zones and at different delay times. In 2D image spectra, the ICCD detector operates in imaging mode and produces an intensity-wavelength plot for each pixel of the detector

at different points in space along the axial direction (plume expansion or propagation direction). In our experimental setup, the 2D spectral imaging technique provides spatial resolution near double the size of the ICCD detector pixel size due to 1:0.5 plasma imaging magnification onto the spectrometer slit.

Fig. 6a and b. Close to here

Fig. 6a and b shows an axial space-resolved imaging and spectrum (a) of the sample plasma at delays of 0 and 500 ns. The recorded spectral intensity is indicated by a pseudo-colour. We observe the same species that we have previously observed at short delay times (see Figs. 3 and 4). Carbon line emission is significant until ≈ 16 mm while ionic line emissions are observed until ≈ 12 mm. We see the spatial displacement of the different species from the target. Moreover the ionic species disappear from the vicinity of the target at 500 ns.

Fig. 7a and b. Close to here

Fig. 7a and b displays the spectra emitted from the sample-plasma at different spatial distances from the target at the same delays than before. It is also shown in the insets of these figures the trend with the distance from the target of the intensity of some representative emission lines. For short delay times ≤ 100 ns (Fig. 7a), the ionized emission intensities in the plasma are greatest in the region close to the target surface and decreases within a few millimeters away from the target. In the region close to the target surface, the density in the plasma core is fairly high. The spectral line from C atoms with long-range spatial distribution shows a maximum at 4 mm. At 500 ns (Fig. 7b), this distribution moves away from the target showing the maximum at 7 mm. A similar behaviour is observed for ionic species with different maxima. Neutral carbon atom shows its maximum later and farther from the target with respect to ions. That indicates that carbon atoms are mainly formed by gas phase recombination of ionized species during the propagation of

the plasma plume. Propagation velocities of ions in a plasma are governed by space-charge effects where highly charged ions possess higher velocities [65].

The peak positions of these plots at different distances from the target surface give information on the propagation of the excited species. As an example, Fig. 8 displays the number density profiles of C^{3+} line at 252.13 nm as a function of distance from the target surface at two delays from the laser pulse. By tracking the maximum brightness or intensity displacement, for different plasma species, gives their average velocities. The expansion velocities of C, C^+ and C^{3+} were found to be 6.1, 9.3 and 12 km/s, respectively. The expansion velocities of the ionized species towards the longitudinal direction are found to be increasing with ionization stage.

Fig. 8. Close to here

In order to estimate some plasma parameters such as electron density and temperature, as well as the dynamics of some species, we study LPP spectra in different spectral regions. Fig. 9 shows the temporal evolution of the LPP sample plasma in the spectral region 272-286 nm monitored at several delays and z= 2 mm.

Fig. 9. Close to here

These spectra are dominated by the C^+ doublet structure around 283.7 nm ($2s^23p\ ^2P_{3/2,\ 1/2} \rightarrow 2s2p^2\ ^2S_{1/2}$) and the two Mg^+ resonance lines at 279.55 and 280.27 nm ($3p\ ^2P_{3/2,\ 1/2} \rightarrow 3s\ ^2S_{1/2}$). For short delays ($t_d \leq 0.1$ μs), the continuum emission significantly contributes to the total emission. As the delay increases, this emission, essentially due to the radiative recombination between electrons and ions and bremsstrahlung emission, drops significantly as a result of the decay of the plasma. Spectrum narrowing was observed with increasing delay as the consequence of the decrease of the temperature and electron density.

The TOF optical distribution of Mg$^+$ (244.956 nm) species has been displayed in Fig. 5. It consists of one intense maximum at 0 μs. However, in Fig. 9 the two Mg$^+$ resonance lines at 279.55 and 280.27 nm show a big maximum at 0 μs and approximately another weak maximum at 0.4 μs. These facts show an anomalous behaviour for the Mg$^+$ species, possibly due to an overlapping of the Mg$^+$ at 244.956 nm (Fig. 5) with some oxygen ionic species and a self- absorption of the two Mg$^+$ resonance lines at 279.55 and 280.27 nm (Fig. 9). This double peak structure observed in vacuum revealed a fast and a slow component in the velocity of Mg$^+$ resonance species. The fast component with a narrow velocity profile can be attributed to the production of these species from the target by electron impact ionization (e + hυ + Mg → e* + Mg → Mg$^+$ + 2e). The slowest component actually emerges due to three-body electron-ion recombination (2e + Mg^{2+} → Mg$^+$ + e). A multiple peak structure has been found by Harilal *et al* [70] in graphite plumes propagating in a helium ambient atmosphere. They attributed to a stratification of plasma into fast and slow ion components occurring at the interface where fast component penetrates the ambient gas and slow one decelerate.

The emission spectra reveal line broadening. This broadening has several components, the most important are the Doppler broadening, the instrumental and the Stark broadening due to the presence of electrons and ions. The Stark effect is the primary mechanism influencing these LPP spectra. The Doppler broadening can be obtained as $\Delta\lambda^{D}_{FWHM} = 7.16\times10^{-6}\times\lambda\times(T/M)^{1/2}$, being λ the line wavelength, T the temperature in K, and M the atomic mass in amu. In these experiments $\Delta\lambda_{instrument}$ was ≈ 0.01 nm estimated by measuring the FWHM of the Cu/Ne lines emitted by a hollow-cathode lamp. One powerful spectroscopic technique to estimate the electron density with reasonable accuracy is by the measurements of the Stark broadened line width of an isolated atom or singly charged ion [1-4]. The FWHM of the Stark broadened line profile $\Delta\lambda^{S}_{FWHM}$ for neutral atoms or singly charged ions, after neglecting the ion-contribution to the broadening, is related to the electron density by the expression [67, 71]

$$\Delta\lambda^{S}_{FWHM} = 2W\left(\frac{n_e}{n_r}\right), \tag{1}$$

where W is the Stark electron impact broadening parameter which can be incorporated to different temperatures [71], n_e is the electron density in cm^{-3} and n_r is the reference electron density ($n_r=10^{16}$ cm^{-3} for neutral atoms and $n_r=10^{17}$ cm^{-3} for singly charged ions). The measurement of the electron density utilizing the Stark component of emission spectral line requires extraction of the Lorentzian component (FWHM) from the lines together with knowledge of the Stark broadening parameters for the lines. This was done by fitting the emitted line profile to a Voigt function and by subtracting Doppler and instrumental line broadening. For the electron density measurements we use the line widths of the C$^+$ line (283.7 nm; $2s^23p\ ^2P^0_{1/2,\ 3/2} \rightarrow 2s2p^2\ ^2S_{1/2}$). By substituting the Stark line widths of C$^+$ doublet at different delay times in Eq. (1) and the electron ion parameter, W (0.0119-0.00678 nm from Griem [71] at temperatures between 5,000 and 40,000 K), we obtain the electron density. The impact parameter is a function of the electron temperature, but the dependence is negligibly weak [66, 71]. Fig. 10 gives the time evolution of electron density for different delays. The insert pictures show two measured C$^+$ line (283.7 nm) spectra at 0 and 1.1 μs and the corresponding fits to a Voigt function. The errors provided for electron densities considered the uncertainty in the impact parameters and line broadenings. We see that the C$^+$ doublet centered at 283.7 nm can partially be resolved at high delays.

Fig. 10. Close to here.

The measurements were made from spectral region shown in Fig. 9. With increasing delay time, the electron density varied from 1.17×10^{18} cm^{-3} at 0 μs to 5.4×10^{17} cm^{-3} at 1.5 μs. The electron density shows rapidly decreasing behavior for short delays ($t_d \leq 0.1$ μs) and then remains more or less steady during the first microsecond. For $t_d > 1$ μs, n_e rapidly decreases as the time is further increased. The decrease of electron density with time is mainly due to recombination between electrons and ions in the plasma. These electron density values are reasonable considering that this

11

density depends on the delay time from the laser pulse, observation distance and the laser pulse duration and laser wavelength.

Figs. 11a and b show the 2D spectral imaging in the spectral region $\approx$ 272-285 nm recorded at different delay times. This region is relevant because the emission intensity of several lines of Mg, Mg^+ and Mg^{2+} is significant and Mg is an important component of the tissue samples.

Fig. 11a and b. Close to here

The maximum intensity of the Mg^+ line at 279.55 nm was located at 7 mm and the peak of the C^+ line at 283.7 nm at 5 mm.

The average expansion velocities for Mg^+ and Mg^{2+} species were calculated by measuring each maximum brightness displacement in the spectra taken at different delay times. The measurements of expansion velocities are limited up to 0.5 μs after plasma formation. By measuring the maximum brightness displacement for Mg^+ and Mg^{2+} species their corresponding average expansion velocities were found to be 5 and 8 km/s, respectively. By comparing these velocities to the ones obtained from carbon species (6.1, 9.3 and 12 km/s for C, C^+ and C^{3+}) we can see that higher velocities correspond to the species with higher ionization degree and lower atomic mass. These velocities should be regarded as an effective stream velocity in the direction normal to the target surface.

Fig. 12 shows the spatially resolved profiles of the electron density along the axial direction at several delays from the laser pulse. These time- and space-resolved profiles were measured from the Stark broadening of the C^+ line at 283.7 nm. In the observed spatial region the electron number density is approximately decreasing with delay time due electron-ions recombination. As it is shown in Fig. 12, at the three observation delays, the electron density can be considered constant along the plume expansion axis except for some shallow minimum. This behavior could be interpreted in terms of electron-ions recombination processes occurring in regions with high species number density [62].

Fig. 12. Close to here

Under the assumption of local thermodynamic equilibrium, the intensities of a set of isolated C^+ lines were used to evaluate the electron temperature at different delay times, Fig. 13. The electron temperature T_e was obtained according to the well-known Boltzmann plot method [1-4] from the time-resolved spectrum. The spectral line wavelengths, the energies of the upper levels, statistical weights, and transition probabilities used for these lines were obtained from NIST [54] and listed in Table 1. An example of this plot is shown in the inset of Fig. 13.

Fig. 13. Close to here
Table 1

At shorter times, continuum emission dominates the emission spectra and the electron temperature measurement is sensitive to the line-continuum ratio. Therefore the electron temperature at shorter time has the higher error and results practically equal to the electron temperature at 100 ns. After this time, the temperature decreases approximately linearly.

4. Conclusions

The laser-induced plasma of swine muscle tissue sample generated by CO_2 laser pulses at 10.591 μm has been investigated spatially and temporally by OES. The emissions observed are mainly due to electronic relaxation of excited neutral Na, K, C, Mg, H, Ca, N and O atoms, ionized C^+, C^{2+}, C^{3+}, Mg^+, Mg^{2+}, N^+, N^{2+}, Ca^+, O^+ and O^{2+} species and molecular band systems of CN, C_2, CH, NH, OH, and CaOH. The main efforts of this work have been concentrated on the spatial and temporal study of 2D OES data. Average velocities of some plasma species were reported. The expansion velocity of various plasma species (Carbon and Magnesium) is related to their charge states as well as their atomic masses. The species with higher ionization and lower

atomic weight move with high velocities compared to their counterparts with lower charge states and higher mass. Spatial and temporal electron densities have been reported by using the Stark broadening method. The electron temperature, calculated by means of Boltzmann diagram plot, decreases with the delay time practically linearly.

Acknowledgments

References

[1] D.A. Cremers, L.J. Radziemski, Handbook of Laser-Induced Breakdown Spectroscopy, Wiley, New York, 2006.

[2] A.W. Miziolek, V. Palleschi, I. Schechter, Laser-Induced Breakdown Spectroscopy, Cambridge University Press, Cambridge, 2006.

[3] J. P. Singh, S.N. Thakur, Laser-Induced Breakdown Spectroscopy, Elsevier, New York, 2007.

[4] S. Musazzi, U. Perini, Laser-Induced Breakdown Spectroscopy. Theory and Applications. Springer, Vol 182, Heidelberg, 2014.

[5] D. Chrisey, G.K. Hubler, Pulsed Laser Deposition of Thin Films, vol. 154–155. Wiley, New York, 1994.

[6] C.R. Phipps, Pulsed Laser Deposition of Thin Films, Springer Verlag, Santa Fe, 2006.

[7] F.C. De Lucia Jr., R.S. Harmon, K.L. McNesby, R.J. Wonkel Jr., A.W. Miziolek, Laser-induced breakdown spectroscopy analysis of energetic materials, Appl. Opt. 42 (2003) 6148–6152.

[8] A. Portnov, S. Rosenwaks, I. Bar, Emission following laser-induced breakdown spectroscopy of organic compounds in ambient air, Appl. Opt. 42 (2003) 2835–2842.

[9] C. Lopez-Moreno, S. Palanco, J.J. Laserna, F.C. DeLucia Jr., A.W. Miziolek, J. Rose, R.A. Walter, A.I. Whitehouse, Test of stand-off laser-induced breakdown spectroscopy sensor for the detection of explosive residual on solid surface, J. Anal. At. Spectrom. 21 (2006) 55–60.

[10] Q. Wang, P. Jander, C. Fricke-Begemann, R. Noll, Comparison of 1064 nm and 266 nm excitation of laser-induced plasmas for several types of plastics and one explosive, Spectrochim. Acta Part B, 63 (2008) 1011-1015.

[11] V. Lazic, A. Palucci, S. Jovicevic, C. Poggi, E. Buono, Analysis of explosive and other organic residues by laser induced breakdown spectroscopy, Spectrochim. Acta Part B, 64 (2009) 1028-1039.

[12] P. Lucena, A. Doña, L.M. Tobaria, J.J. Laserna, New challenges and insights in the detection and spectral identification of organic explosives by laser induced breakdown spectroscopy, Spectrochim Acta Part B, 66 (2011) 12-20.

[13] Q. Wang, K. Liu, H. Zhao, C.H. Ge, Z.W. Huang, Detection of explosives with laser-induced breakdown spectroscopy, Front. Phys. 7 (2012) 701-707.

[14] M.A. Gondal, T. Hussain, Z. Ahmad, A. Bakry, Detection of contaminants in ore samples using laser-induced break down spectroscopy, Journal of Environmental Sciences and Health Part A, 42 (2007) 879-887.

[15] T. Hussain, M.A. Gondal, Detection of toxic metals in waste water from dairy products plant using laser-induced breakdown spectroscopy, Bulletin of environmental contamination & toxicology, 80 (2008) 561-565.

[16] C. Lopez-Moreno, S. Palanco, J.J. Laserna, Remote Laser-Induced Plasma Spectrometry for Elemental Analysis of Samples of Environmental Interest. J. Anal. At. Spectrom. 19 (2004), 1479-1484.

[17] A. Giardini, V. Marotta, A. Morone, S. Orlando, G.P. Parisi, Thin films deposition in RF generated plasma by reactive pulsed laser ablation, Appl. Surf. Sci. 197 (2002) 338–342

[18] T. Guo, P. Nikolaev, A.G. Rinzler, D. Tomanek, D.T. Colbert, R.E. Smalley, Self-assembly of tubular fullerenes, J. Phys. Chem. 99 (1995) 10694–10697.

[19] C. Fotakis, D. Anglos, V. Zafiropulos, S. Georgiou, V. Tornari, Lasers in the Preservation of Cultural Heritage: Principles and Applications, Taylor & Francis, New York, 2007.

[20] R. Brennetot, J.L. Lacour, E. Vors, A. Rivoallan, D. Vailhen, S. Maurice, (2003) Mars analysis by laser-induced breakdown spectroscopy (MALIS): Influence of mars atmosphere on plasma emission and study of factors influencing plasma emission with the use of Doehlert designs. Appl. Spectrosc. 57 (2003) 744-752.

[21] L. Radziemski, D. Cremers, K. Benelli, C. Khoo, R.D. Harris, Use of the vacuum ultraviolet spectral region for LIBS-based Martian geology and exploration. Spectrochimica Acta Part B, 60 (2005) 237-248.

[22] B. Salle, D.A. Cremers, S. Maurice, R.C. Wiens, Laser-induced breakdown spectroscopy for space exploration applications: Influence of ambient pressure on the calibration curves prepared from soil and clay samples. Spectrochim. Acta Part B, 60 (2005) 479-490.

[23] M. Baudelet, M. Boueri, J. Yua, S.S. Mao, V. Piscitelli, X. Mao, R.E. Russo, Time-resolved ultraviolet laser-induced breakdown spectroscopy for organic material analysis, Spectrochim. Acta Part B, 62 (2007 1329-1334.

[24] J.L. Gottfried, F.C. DeLucia, C.A. Munson, A.W. Miziolek, Standoff detection of chemical and biological threats using laser-induced breakdown spectroscopy, Appl. Spectrosc. 62 (2008) 353-363.

[25] C.R. Dockery, S.R. Goode, Laser-induced breakdown spectroscopy for the detection of gunshot residues on the hands of a shutter, Appl. Opt. 42 (2003) 6153-6168.

[26] A. C. Samuels, F. C. DeLucia, K.L. McNesby, A.W. Miziolek, Laser-induced breakdown spectroscopy of bacterial spores, molds, pollens, and protein: Initial studies of discrimination potential. Appl. Opt. 42 (2003), 6205–6209.

[27] C. A. Munson, F. C. De Lucia, T. Piehler, K. L. McNesby, A. W. Miziolek, Investigation of statistics strategies for improving the discrimination power of laser-induced breakdown spectroscopy for chemical and biological warfare agent simulants, Spectrochim. Acta Part B 60 (2005) 1217-1224.

[28] C. A. Munson, J. L. Gottfried, E. G. Snyder, F. C. De Lucia, B. Gullett, A. W. Miziolek, Detection of indoor biological hazards using the man-portable laser induced breakdown spectrometer. Appl. Opt. 47 (2008), 48–57.

[29] A. Vogel, V. Venugopalan, Mechanisms of pulsed laser ablation of biological tissues, Chem. Rev. 103 (2003) 577-644.

[30] S. J. Rehse, H. Salimnia, A. W. Miziolek, Laser-induced breakdown spectroscopy (LIBS): an overview of recent progress and future potential for biomedical applications, Journal of Medical Engineering & Technology, 36 (2012) 77–89.

[31] J. Kaiser, K. Novotny, M.Z. Martin et al, Trace elemental analysis by laser-induced breakdown spectroscopy—Biological applications, Surface Science Reports 67 (2012) 233–243.

[32] D. Santos, R.E. Samad, L.C. Trevizan, A.Z. de Freitas, N.D. Vieira, F.J. Krug, Evaluation of femtosecond laser-induced breakdown spectroscopy for analysis of animal tissues, Appl Spectrosc. 62 (2008) 1137-1143.

[33] R. Kanawade, F. Mehari, C. Knipfer, M. Rohde, K. Tangermann-Gerk, M. Schmidt, and F. Stelzle, Pilot study of laser induced breakdown spectroscopy for tissue differentiation by monitoring the plume created during laser surgery – An approach on the feedback laser control mechanism, Spectrochim. Acta, Part B, 87 (2013) 175-181.

[34] F. Stelzle, I. Terwey, C. Knipfer, W. Adler, K. Tangermann-Gerk, E. Nkenke, and M. Schmidt, The impact of laser ablation on optical soft tissue differentiation for tissue specific laser surgery-an experimental ex vivo study, J. Transl. Med. 10 (2012) 123-132.

[35] R. Kanawade, F. Mahari, F. Klampfl, M. Rohde, C. Knipfer, K. Tangermann-Gerk, W. Adler, M. Schmidt, F. Stelzle, Qualitative tissue differentiation by analyzing the intensity ratios of atomic emission lines using laser induced breakdown spectroscopy (LIBS): prospects for a feedback mechanism for surgical laser systems, J. Biophotonics 1-9 (2013).

[36] F. Mehari, M. Rohde, C. Knipfer, R. Kanawade, F. Klampfl, W. Adler, F. Stelzle, M. Schmidt, Laser induced breakdown spectroscopy for bone and cartilage differentiation - ex vivo

study as a prospect for a laser surgery feedback mechanism, Biomedical Optics Express, 5 (2014) 4013-4023.

[37] A. Marin-Roldan, S. Manzoor, S. Moncayo, F. Navarro-Villoslada, R.C. Izquierdo-Hornillos, J.O. Caceres, Determination of the postmortem interval by Laser Induced Breakdown Spectroscopy using swine skeletal muscles, Spectrochim. Acta Part B, 88 (2013) 186-191.

[38] S. Morel, N. Leon, P. Adam, J. Amouroux, Detection of bacteria by time-resolved laser-induced breakdown spectroscopy, Appl. Opt. 42 (2003) 6184–6191.

[39] J.D. Hybl, G.A. Lithgow, S.G. Buckley, Laser-induced breakdown spectroscopy detection and classification of biological aerosols, Appl. Spectrosc. 57 (2003) 1207–1215.

[40] T. Kim, Z G. Specht, P.S. Vary, C.T. Lin, Spectral fingerprints of bacterial strains by laser-induced breakdown spectroscopy, J. Phys. Chem. 108 (2004) 5477-5482.

[41] P.B. Dixon, D.W. Hahn, Feasibility of detection and identification of individual bioaerosols usng laser-induced breakdown spectroscopy, Anal. Chem. 77 (2005) 631–638.

[42] M. Baudelet, L. Guyon, J. Yu, J.P. Wolf, T. Amodeo, E. Frejafon, P. Laloi, Spectral signature of native CN bonds for bacterium detection and identification using femtosecond laser induced breakdown spectroscopy, Appl. Phys. Lett. 88 (2006) 063901-13.

[43] M. Baudelet, L. Guyon, J. Yu, J.P. Wolf, T. Amodeo, E. Frejafon, P. Laloi, Femtosecond time-resolved laser-induced breakdown spectroscopy for detection and identification of bacteria: a comparison to the nanosecond regime, J. Appl. Phys. 99 (2006) 084701-9.

[44] M. Baudelet, J. Yu, M. Bossu, J. Jovelet, J.P. Wolf, T. Amodeo, E. Frejafon, P. Laloi, Discrimination of microbiological samples using femtosecond laser-induced breakdown spectroscopy, Appl. Phys. Lett. 89 (2006) 163903-1.

[45] S.J. Rehse, J. Diedrich, S. Palchaudhuri, Identification and discrimination of Pseudomonas aeruginosa bacteria grown in blood and bile by laser-induced breakdown spectroscopy, Spectrochim. Acta, Part B, 62 (2007) 1169-1176.

[46] M. Baudelet, M. Boueri, J. Yu, S.S. Mao, V. Piscitelli, X. Mao, R.E. Russo, Time-resolved ultraviolet laser-induced breakdown spectroscopy for organic material analysis, Spectrochim. Acta Part B 62 (2007) 1329–1334.

[47] S.J. Rehse, N. Jeyasingham, J. Diedrich, S. Palchaudhuri, A membrane basis for bacterial identification and discrimination using laser-induced breakdown spectroscopy, J. Applied Phys. 105 (2009) 102034.

[48] S.J. Rehse, Q.I. Mohaidat, S. Palchaudhuri, Towards the clinical application of laser-induced breakdown spectroscopy for rapid pathogen diagnosis: the effect of mixed cultures and sample dilution on bacterial identification, Applied Optics 49 (2010) C27-C35.

[49] V.K. Singh, A.K. Rai, Prospects for laser-induced breakdown spectroscopy for biomedical applications: a review, Lasers Med. Sci. 26 (2011) 673-687.

[50] S.J. Rehse, H. Salimnia, A.W. Miziolek, Laser-induced breakdown spectroscopy (LIBS): an overview of recent progress and future potential for biomedical applications, Journal of Medical Engineering and Technology, 36 (2012) 77-89.

[51] J.J. Camacho, L. Diaz, M. Santos and J.M.L. Poyato, Time-resolved optical emission spectroscopic measurements of He plasma induced by a high-power CO_2 pulsed laser, Spectrochim. Acta Part B, 66 (2011) 57-66.

[52] J.J. Camacho, L. Diaz, J.P. Cid, J.M.L. Poyato, Time-resolved study of the plasma-plume emission during the nanosecond ablation of lithium fluoride, Spectrochim. Acta Part B, 88 (2013) 203-210.

[53] M. D'Orazio, B. Schrader, Calibration of the absolute spectral response of Raman spectrometers, J. Raman Spectrosc. 2 (1974) 585-592.

[54] NIST Atomic Spectra Database online at http://physics.nist.gov/PhysRefData/ASD/index.html, 2008.

[55] J.J. Camacho, M. Santos, L. Diaz, J.M.L. Poyato, Optical emission spectroscopy of oxygen plasma induced by IR CO_2 pulsed laser, J. Phys. D: Appl. Phys. 41 (2008) 215206-13.

[56] J.J. Camacho, L. Diaz, M. Santos, L.J. Juan and J. M. L. Poyato, Temporal evolution of the laser-induced plasma generated by IR CO_2 pulsed laser on carbon targets, J. Appl. Phys. 106 (2009) 033306-11.

[57] J.J. Camacho, L. Diaz, M. Santos, L.J. Juan, J.M.L. Poyato, Time-resolved emission spectroscopy of laser-produced air plasma, J. Appl. Phys. 107 (2009) 083306-9.

[58] J.J. Camacho, L. Diaz, J. P. Cid, J. M. L. Poyato, Time-resolved spectroscopic diagnostic of the CO_2 plasma induced by a high-power CO_2 pulsed laser, Spectrochim. Acta B, 66 (2011) 698-705.

[59] J. Siegel, G. Epurescu, A. Perea, F.J. Gordillo-Vazquez, J. Gonzalo, C.N. Afonso, Temporally and spectrally resolved imaging of laser-induced plasmas, Optics Lett., 29 (2004) 2228-2230.

[60] D. Doria, K.D. Kavanagh, J.T. Costello, H. Luna, Plasma parametrization by analysis of time-resolved laser plasma image spectra, Meas. Sci. Technol. 17 (2006) 1-5.

[61] H. Luna, J. Dardis, D. Doria, J.T. Costello, Analysis of time-resolved laser plasma ablation using an imaging spectra technique, Braz. J. Phys., 37 (2007) 1301-1305.

[62] A. De Giacomo, M. Dell'Aglio, D. Bruno, R. Gaudiuso, O. De Pascale, Experimental and theoretical comparison of single-pulse and double-pulse laser induced breakdown spectroscopy on metallic samples, Spectrochim. Acta B, 63 (2008) 805-816.

[63] M. Chen, X. Liu, M. Zhao, C. Chen, B. Man, Temporal and spatial evolution of Si atoms produced by a nanosecond laser ablating silicon carbide crystals, Phys. Rev., 80 (2009) 016405-6.

[64] A. De Giacomo, M. Dell'Aglio, R. Gaudiuso, G. Cristoforetti, V. Palleschi, E. Tognoni, Spatial distribution of hydrogen and other emitters in aluminium laser-induced plasma in air and

consequences on spatially integrated laser-induced breakdown spectroscopy measurements, Spectrochim. Acta B, 63 (2008) 980-987.

[65] D. Campos, S.S. Harilal, A. Hassanein, Laser wavelength effects on ionic and atomic emission from tin plasmas, Appl. Phys. Lett. 96 (2010) 151501-3.

[66] R.W. Coons, S.S. Harilal, M. Polek, A. Hassanein, Spatial and temporal variations of electron temperatures and densities from EUV-emitting lithium plasmas, Anal. Bioanal. Chem., 400 (2011) 3239-3246.

[67] S.S. Harilal, T. Sizyuk, A. Hassanein, D. Campos, P. Hough, The effect of excitation wavelength on dynamics of laser-produced tin plasma, J. Appl. Phys., 109 (2011) 063306-9.

[68] T. Wu, X. Wang, S. Wang, J. Tang, P. Lu, H. Lu, Time and space resolved visible spectroscopic imaging CO_2 laser produced extreme ultraviolet emitting tin plasma, J. Appl. Phys., 111 (2012) 063304-7.

[69] L. Diaz, J.J. Camacho, J.P. Cid, M. Martin, J.M.L. Poyato, Time evolution of the infrared laser ablation plasma plume of SiO, Appl. Phys. A, 117 (2014) 125-129.

[70] S.S. Harilal, R.C. Issac, C.V. Bindhu, V.P.N. Nampoori, C.P.G. Vallabhan, Emission characteristics and dynamics of C_2 from laser produced graphite plasma, J. Appl. Phys., 81 (1997) 3637-3643.

[71] H.R. Griem, Principles of Plasma Spectroscopy, Cambridge University Press, Cambridge 1997.

Fig. 1. Schematic of the experimental setup.

Fig. 2. An overview of the LPP spectrum of a lyophilized and pellet swine skeletal muscle sample plasma induced by a TEA-CO_2 pulsed laser compared with atomic/ionic lines positions and relative intensities listed in NIST of Na, K, Mg, Mg_+, C, C_+, N, N_+, O and H.

Fig. 3. High-resolution normalized emission spectra from LPP of: (▪) swine sample in vacuum; (−) O_2; (−) air; (−) graphite in N_2 atmosphere (320 hPa); (−) graphite in vacuum**Fig. 4.** Time-resolved emission spectra from laser-induced (123 $J{\times}cm_{-2}$) sample plasma at different delay times (fixed gate width time of 0.1 μs) for z=2 mm. The inset shows a detailed assignment of the spectrum corresponding to a delay of 0 μs.

Fig. 5. Normalized optical TOF distributions of some C, C_+, C_{3+}, N_+, O_{2+}, and Mg_+ lines as a function of delay (fixed gate width time of 0.1 μs) for a laser fluence of 123 $J{\times}cm_{-2}$ and $z = 2$ mm.

Fig. 6a and b. Typical axial space-resolved image of the swine skeletal muscle sample plasma (80 $J{\times}cm_{-2}$) at delays of 0 ns (a) and 500 ns (b) and gate width time of 100 ns. The corresponding spectrum is also shown (a).

Fig. 7a and b. Spatial distribution of the spectra emitted from swine skeletal muscle sample plasma (80 $J{\times}cm_{-2}$) at (a) delay of 0 ns and (b) 500 ns, gate width time of 100 ns. The insets show the relative intensity dependence on distance to surface target for different species.

Fig. 8. Emission profiles of the C_{3+} line at 252.13 nm as a function of distance from the target surface (laser fluence used 80 $J{\times}cm_{-2}$) at 0 and 500 ns delay time.

Fig. 9. Time-resolved emission spectra from laser-induced (123 $J{\times}cm_{-2}$) sample plasma at different delay times (fixed gate width time of 0.1 μs) for z=2 mm. The inset shows the relative intensity dependence on delay time of the plasma ignition for the species Mg_+ (279.55 and 280.27 nm).

Fig. 10. Temporal evolution of electron density from conventional 1D OES (123 $J{\times}cm_{-2}$) sample plasma at a fixed gate width time of 0.1 μs and for z=2 mm. The insets show the experimental emission from C II 283.7 nm at delays of 0 and 1.1 μs and the corresponding Voigt fit.

Fig. 11a and b. Axial space-resolved 2D spectral images of the sample plasma (80 $J{\times}cm_{-2}$) recorded at delay times of (a) 0 ns; (b) 0.5 μs for a gate width time of 0.2 μs.

Fig. 12. Spatial evolution of electron density from 2D OES sample plasma (80 $J{\times}cm_{-2}$) measured at 0, 0.5, and 1 μs delays using a fixed gate width time of 0.2 μs.

Fig. 13. Time evolution of electron temperature after plasma formation. The inset shows a linear Boltzmann plot at 0.3μs delay and z=2 mm with a regression coefficient of 0.97. The gate was set at 100 ns.

Table 1. List of C_+ transition lines and their spectral database used for plasma temperature calculation.
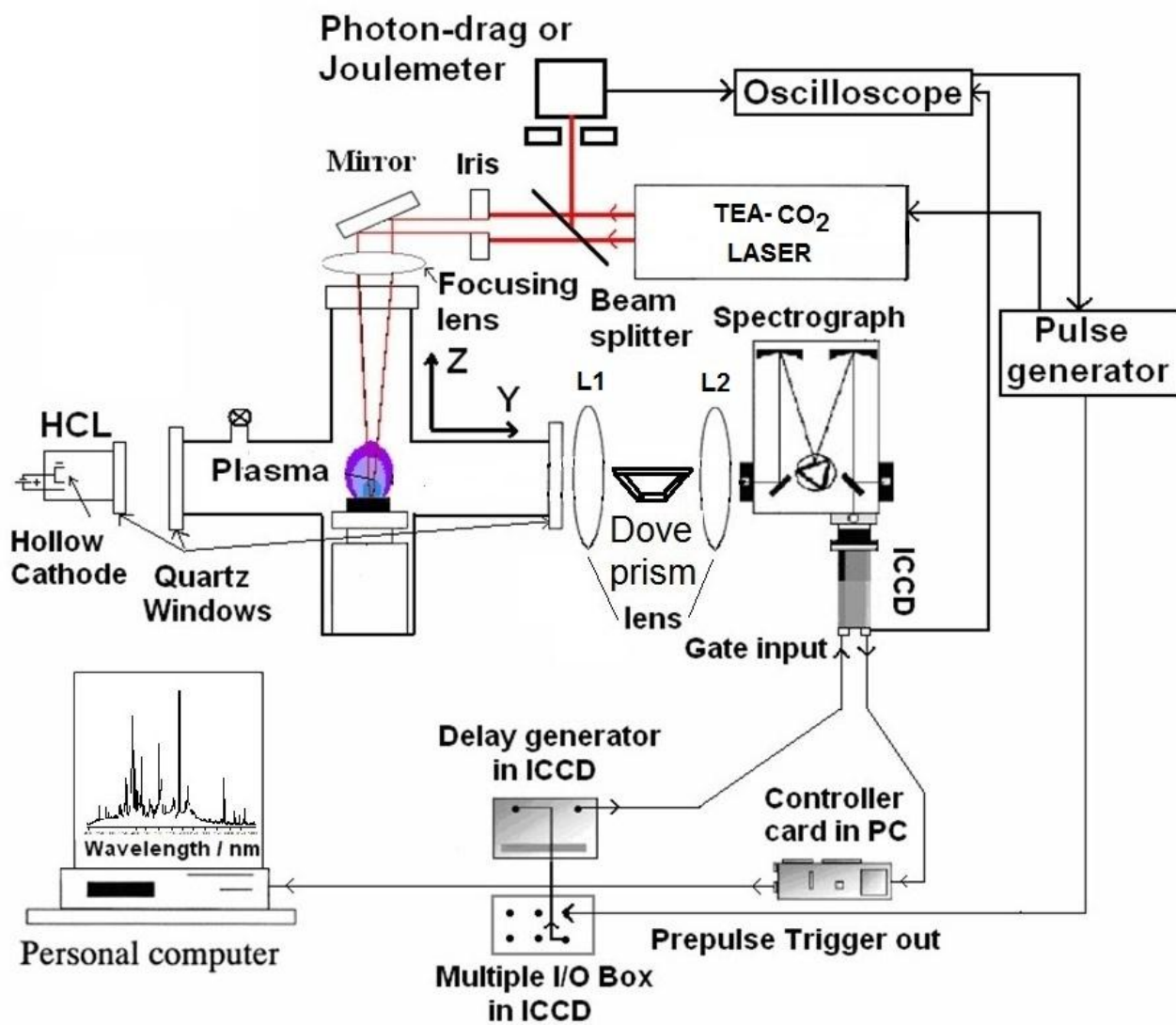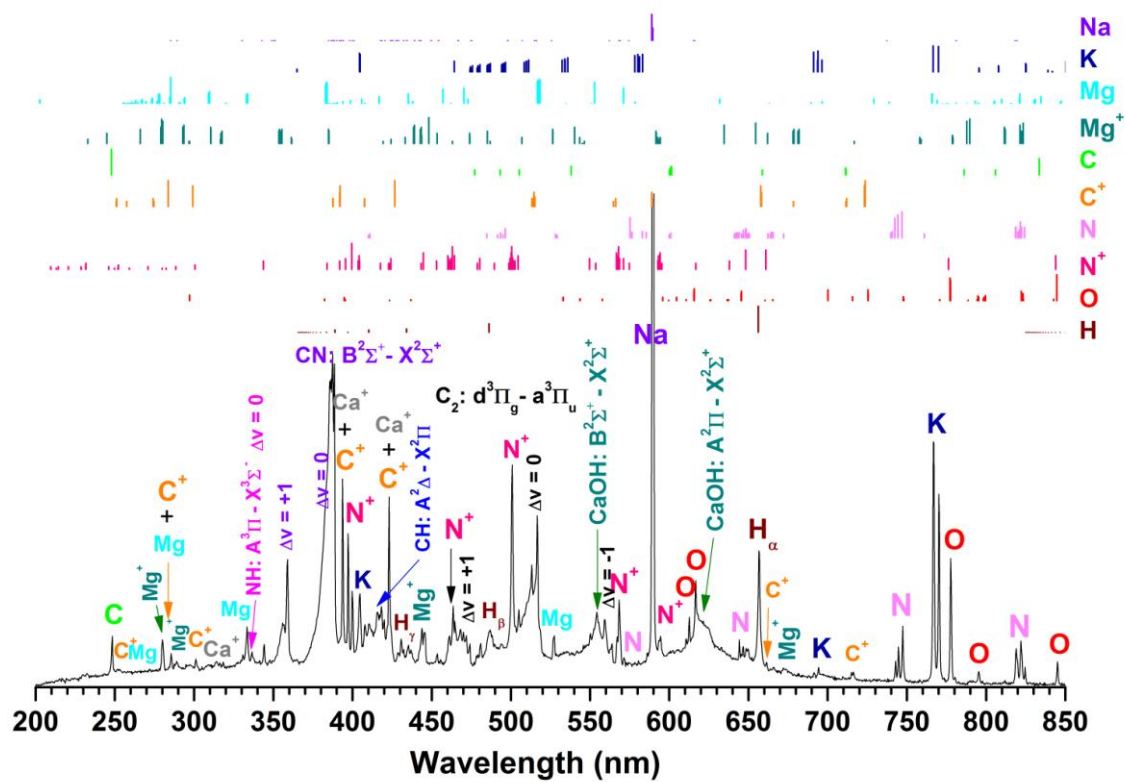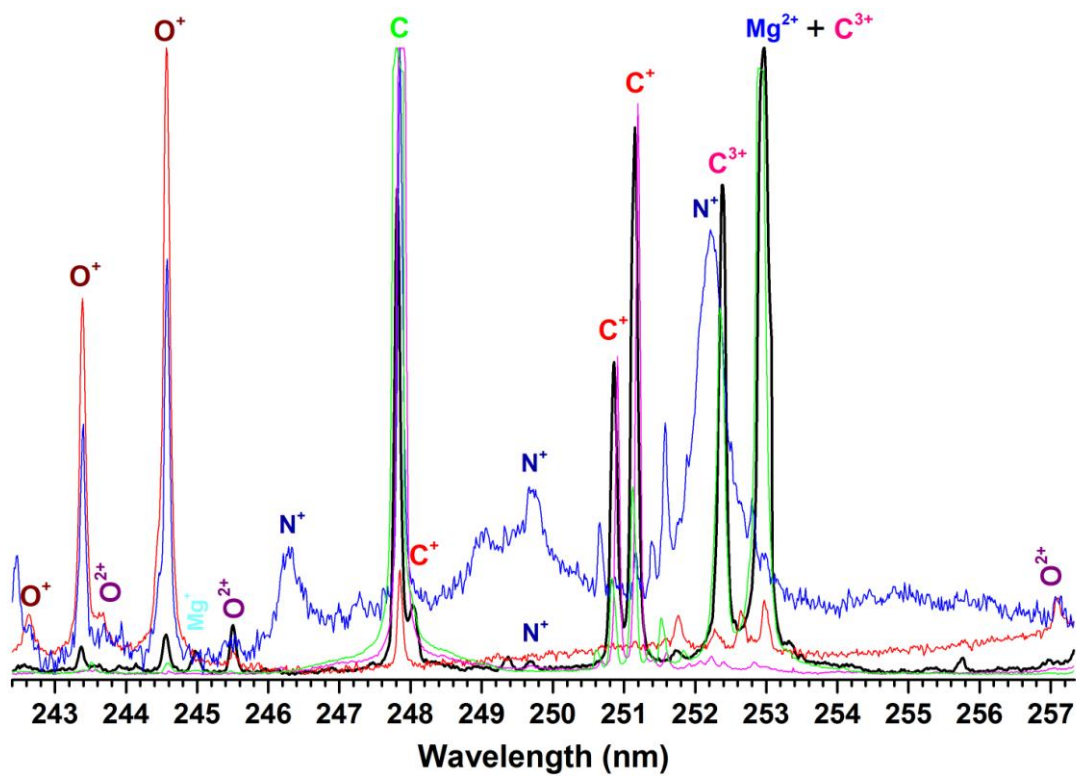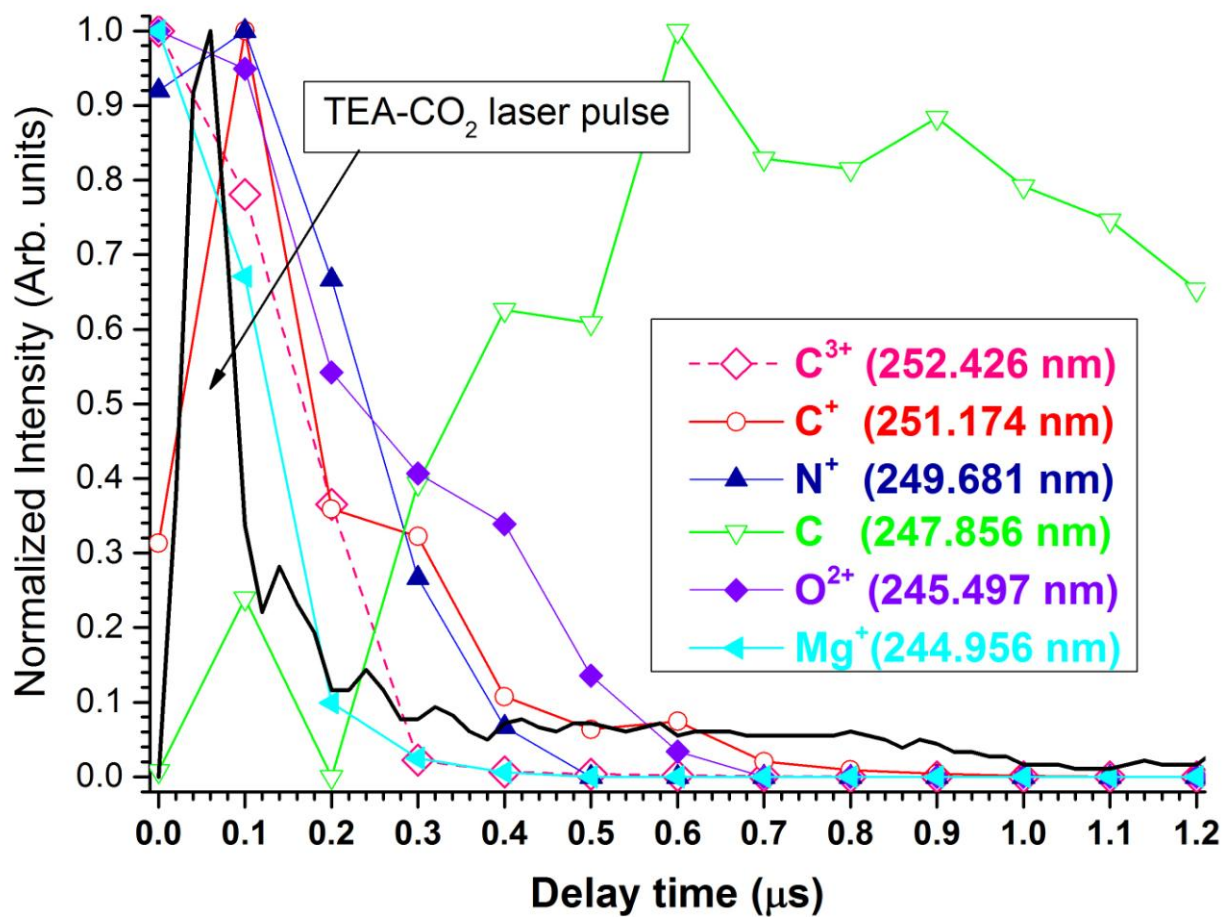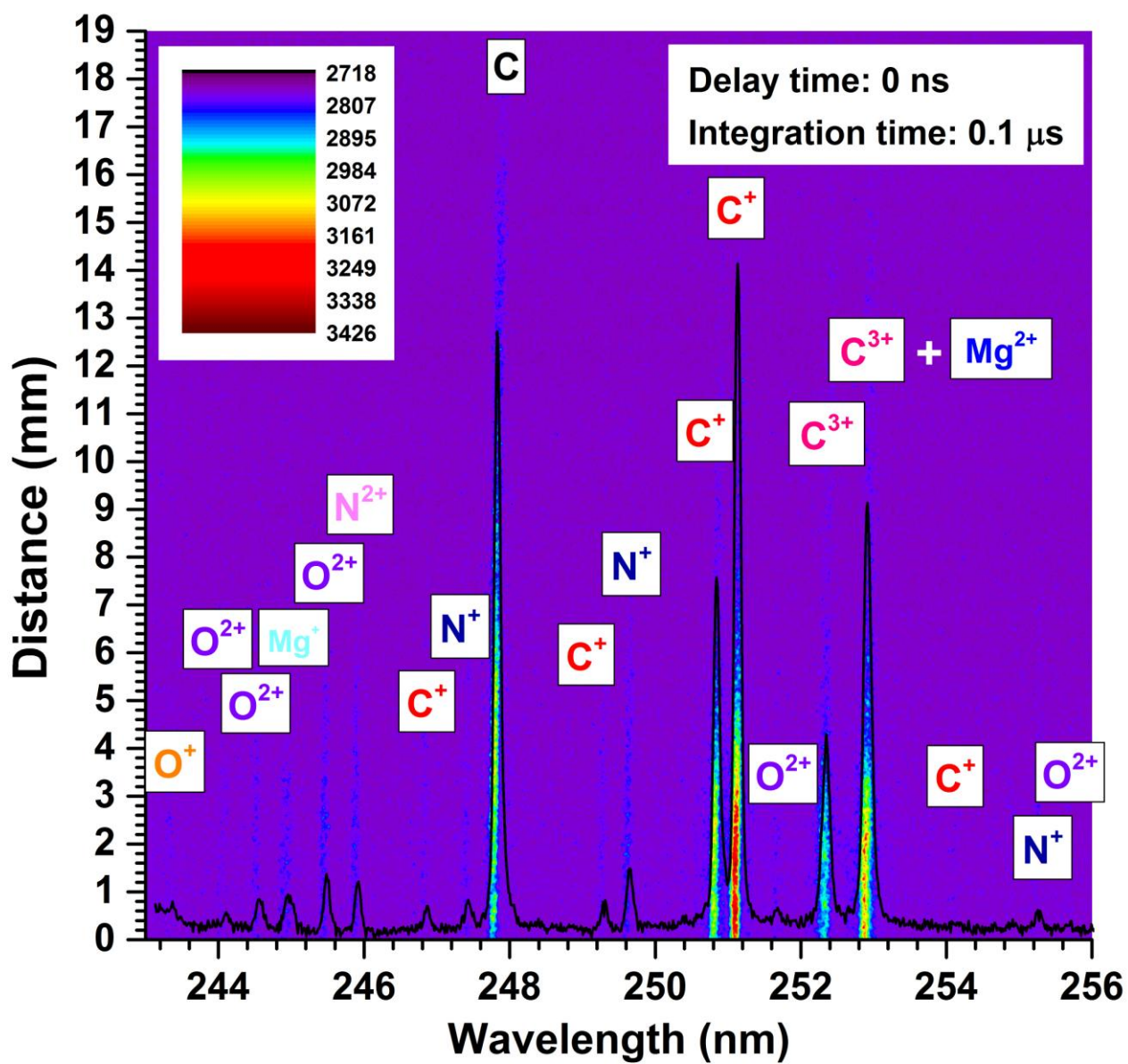
Figure 1

Figure 2

Figure 3

Figure 4

Figure 5

Figure 6a
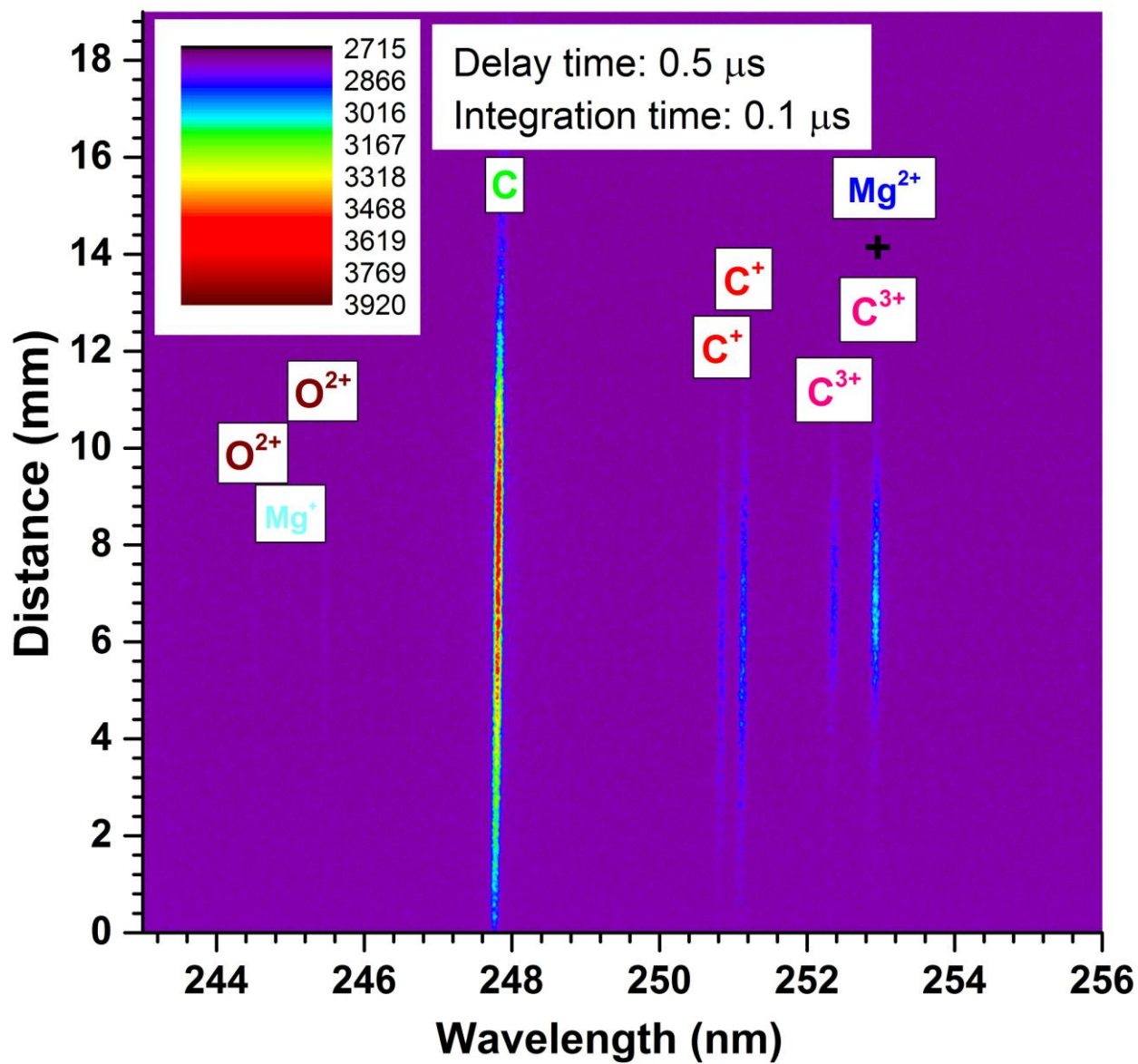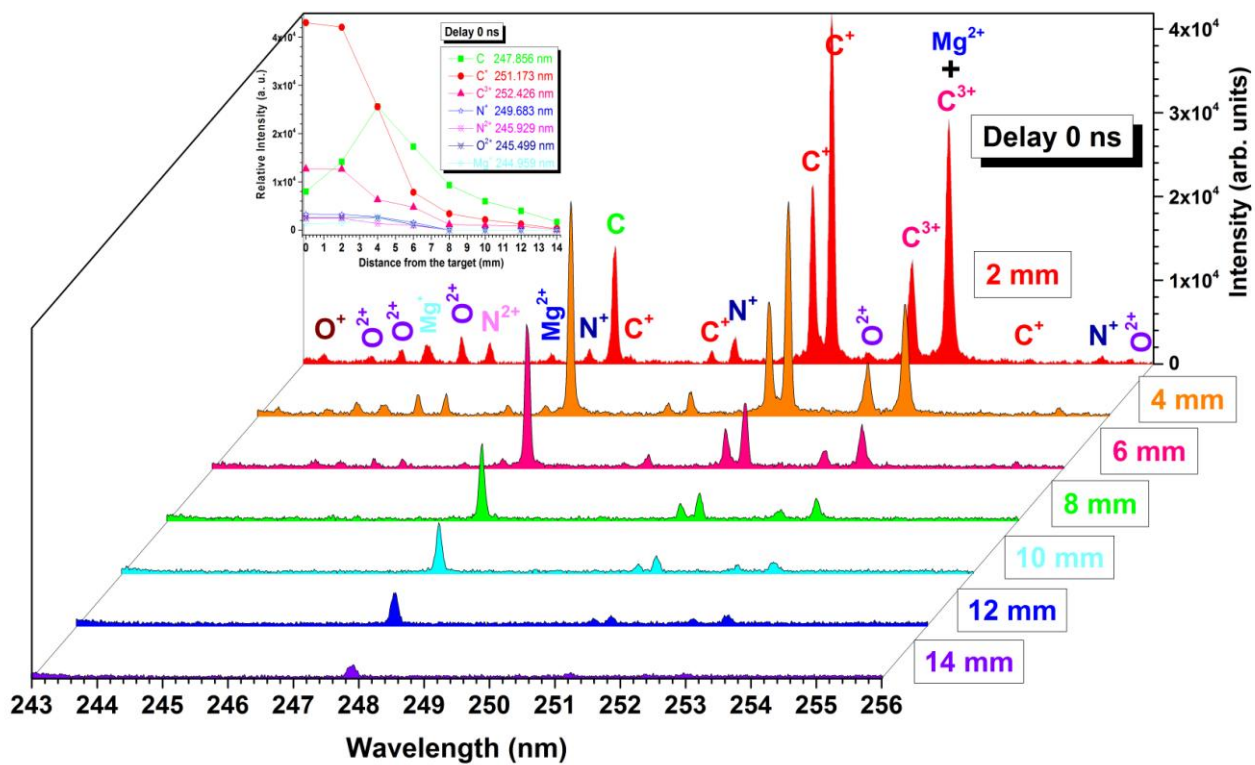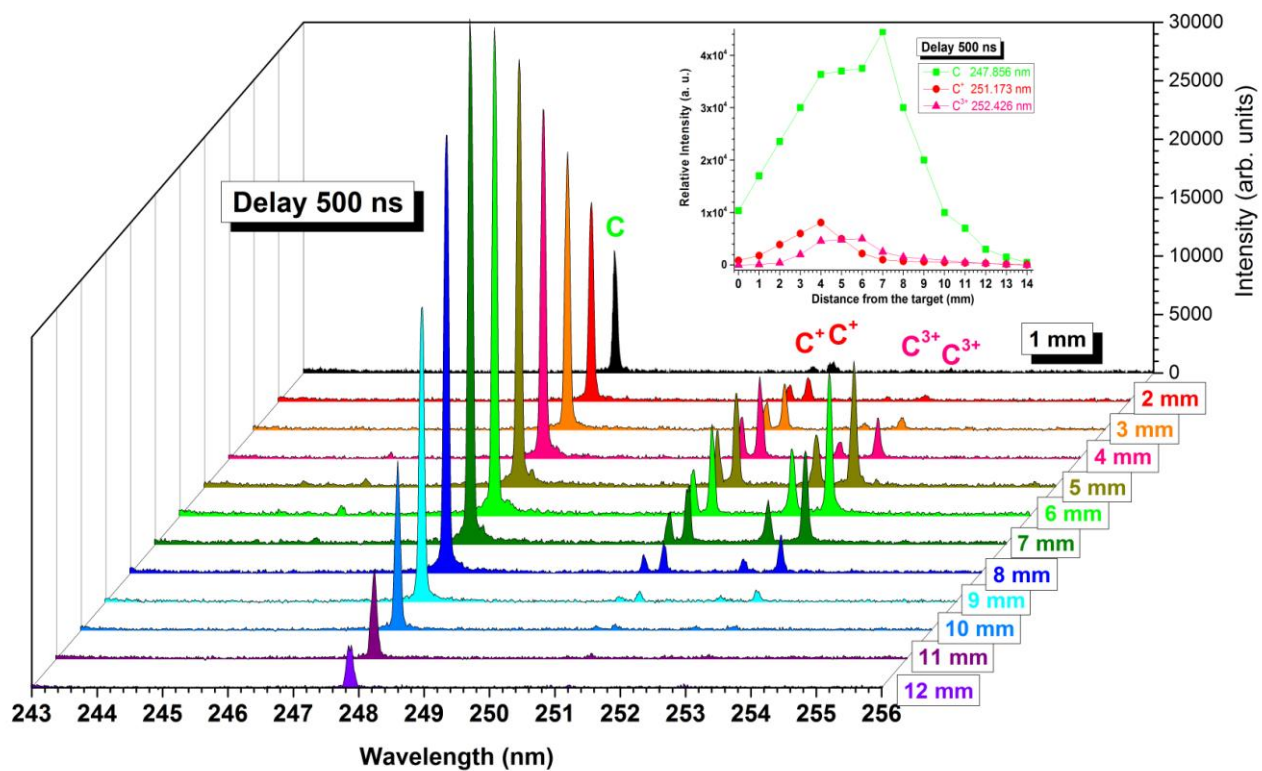
Figure 6b

Figure 7a

Figure 7b

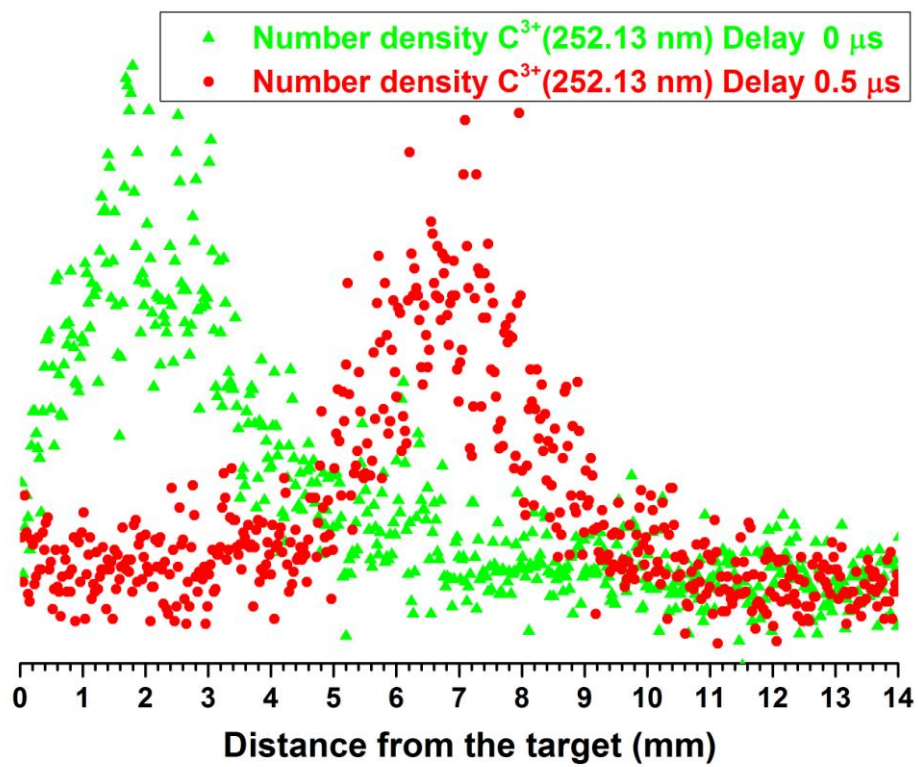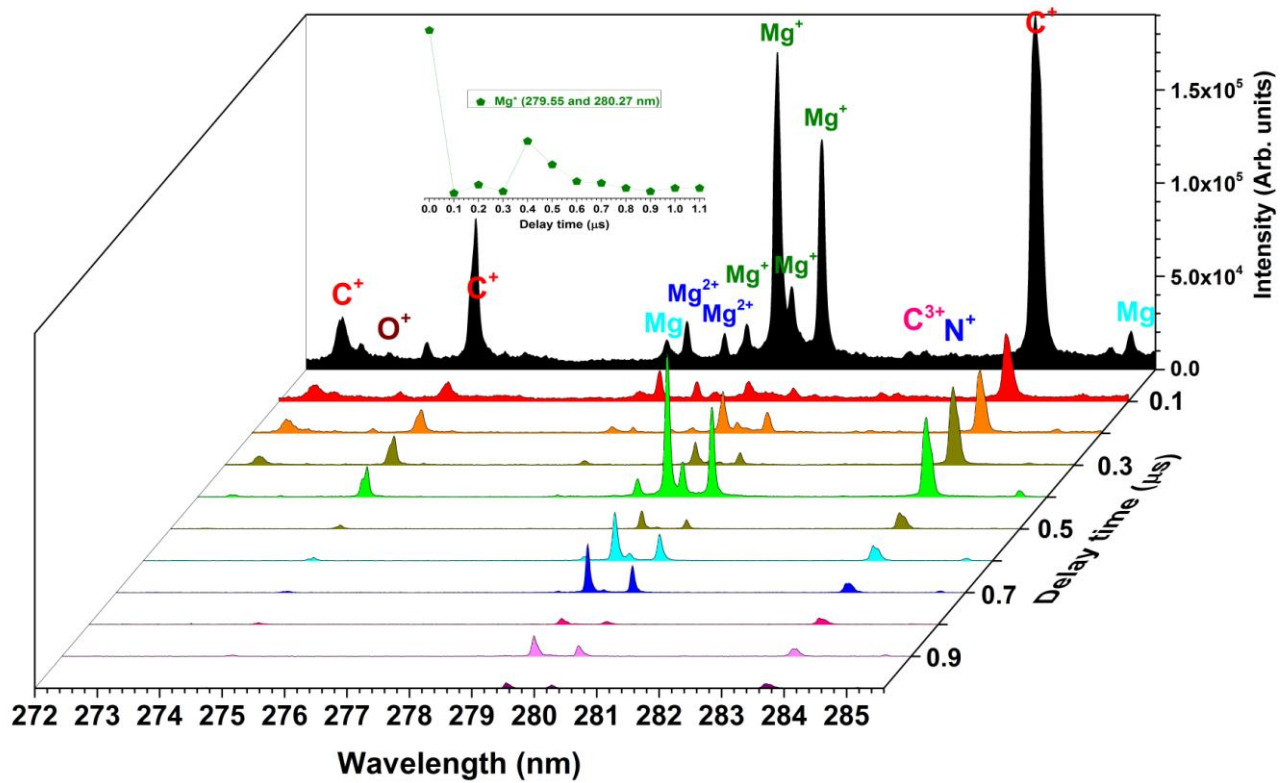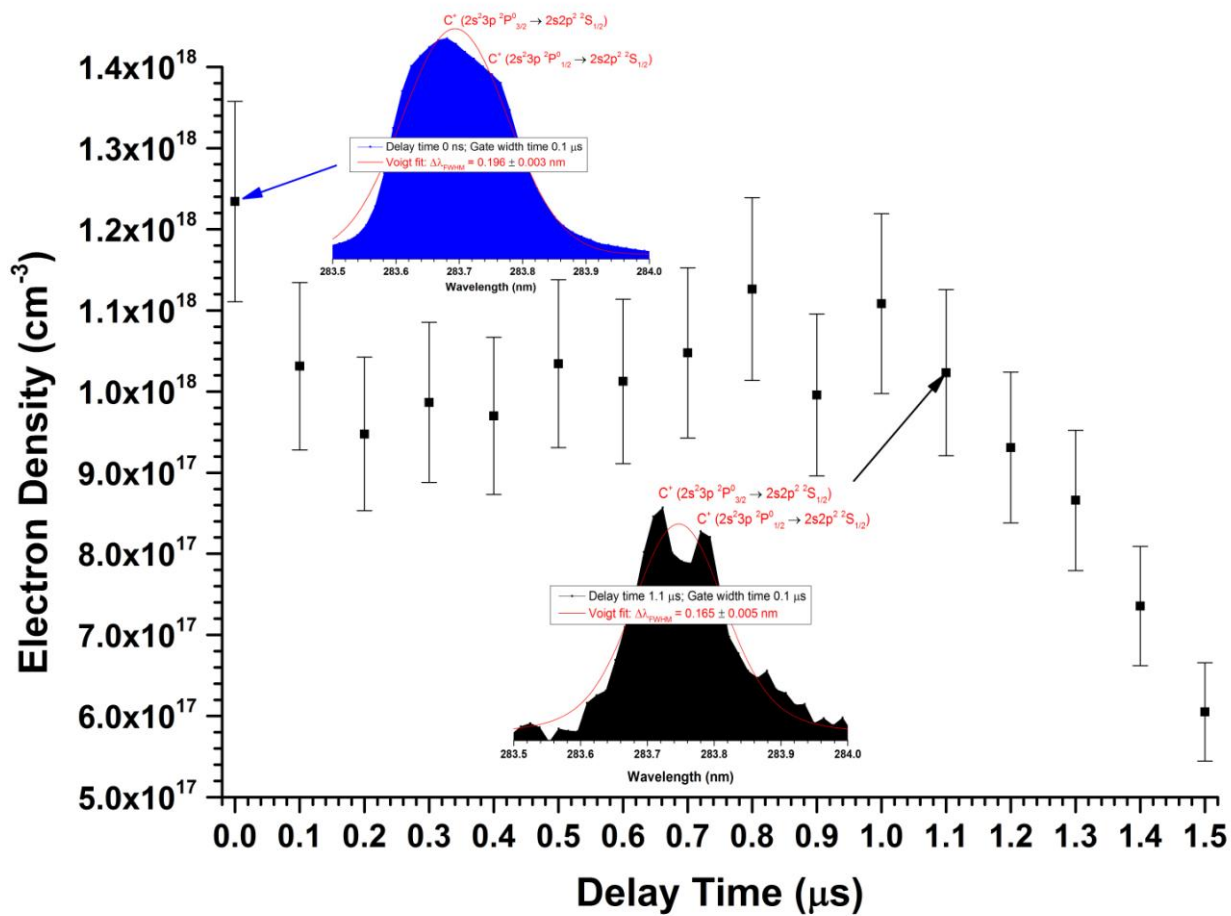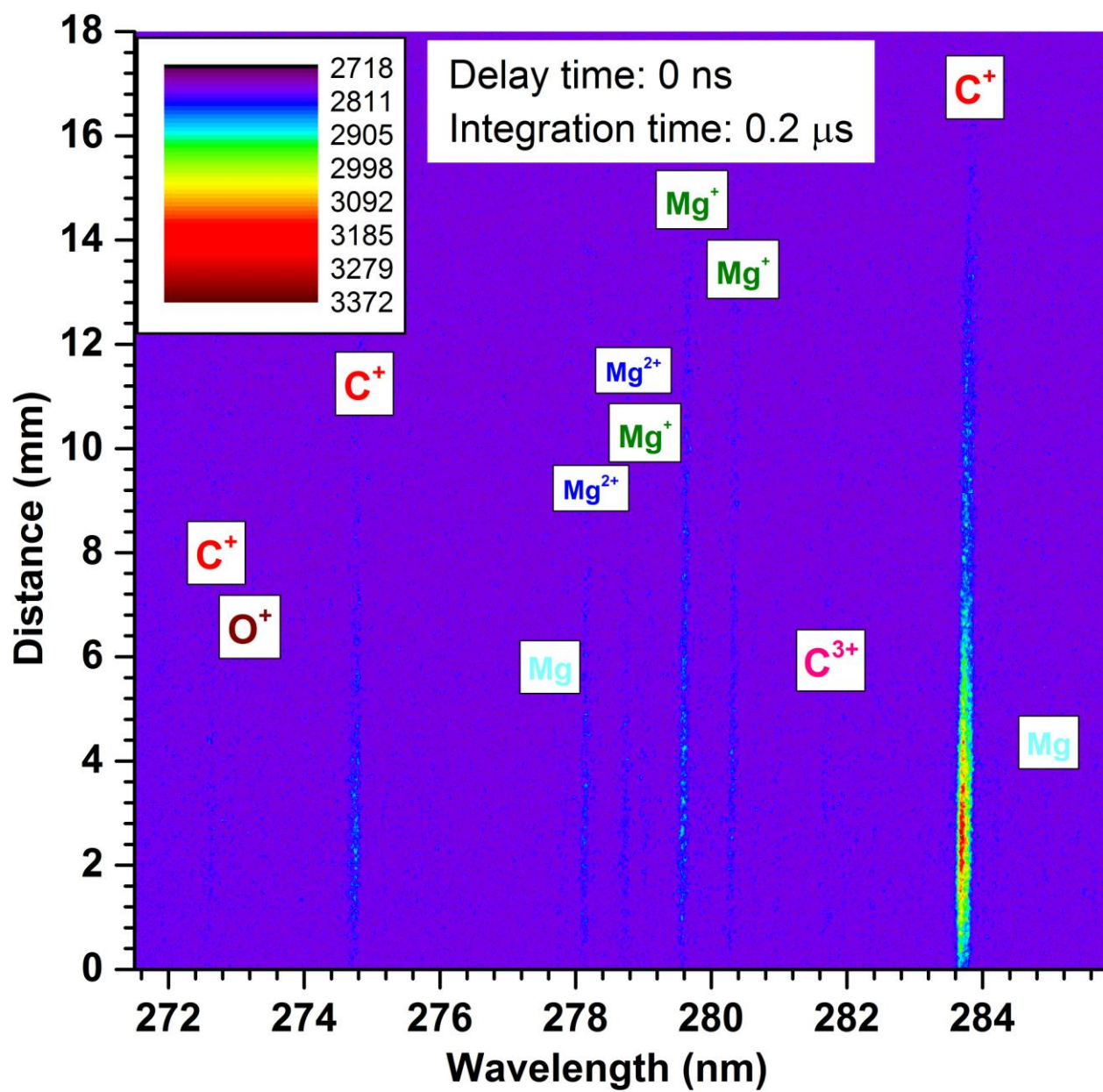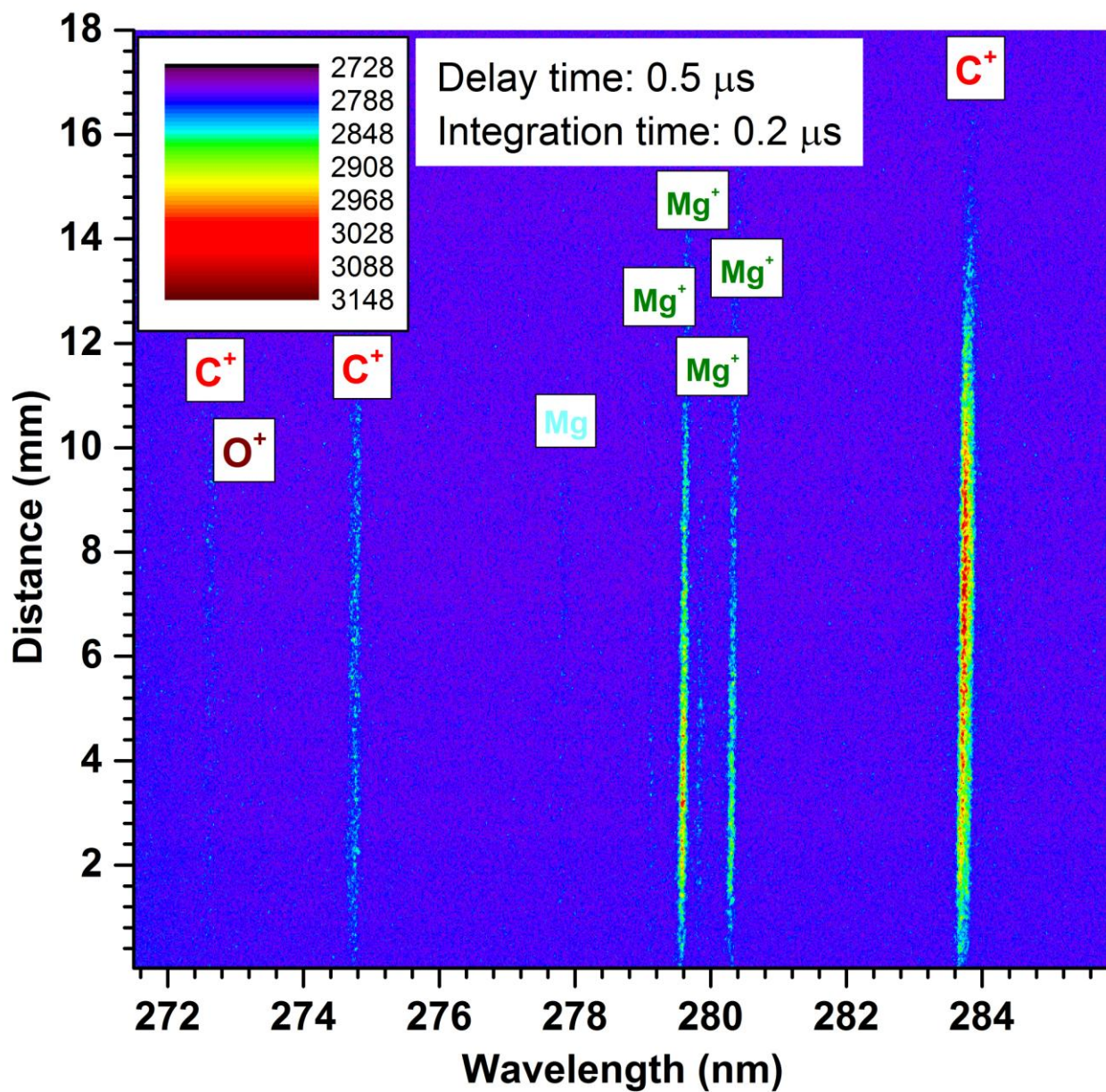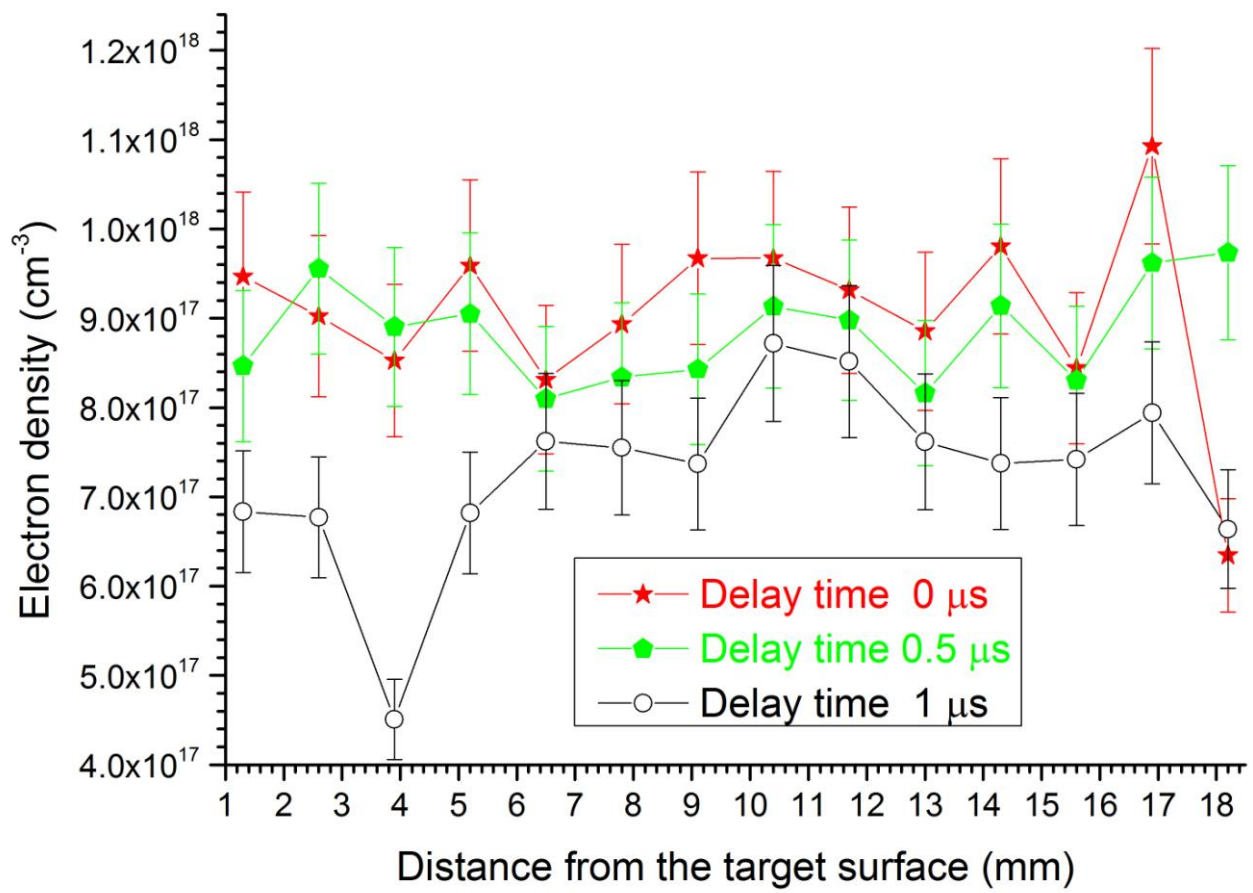Figure 8

Figure 9

Figure 10

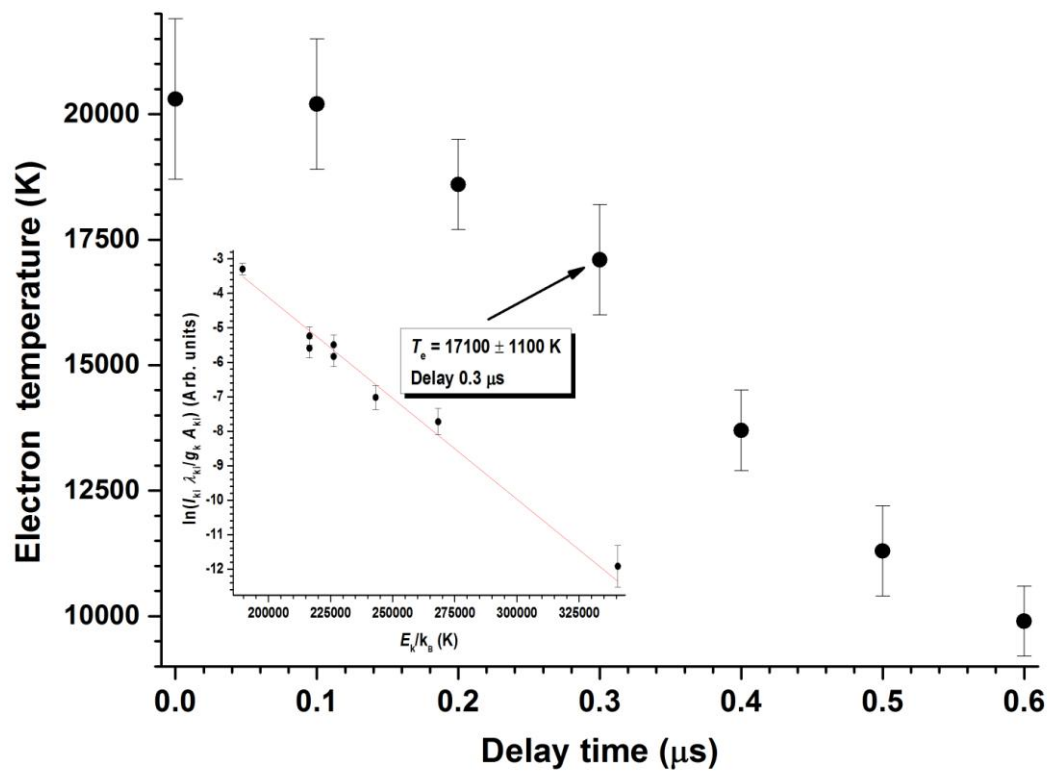Figure 11a

Figure 11b

Figure 12

Figure 13

Table 1.

List of C+ transition lines and their spectral database used for plasma temperature calculation.

Wavelength (nm)	Energy Upper Level (E_k/cm^{-1})	g_k Upper Level	Transition Probability ($A_J 10^8$s^{-1})
249.139	236708.1	10	0.4477
250.913	150466.7	4	0.471
251.174	150461.6	6	0.561
283.671	131735.5	4	0.5744
391.897	157234.1	2	0.6676
392.068	157234.1	2	1.331
426.726	168978.3	8	2.38
513.328	186466.0	6	0.0387

HIGHLIGHTS

LIBS of swine muscle tissue sample generated by CO_2 laser pulses has been done for the first time with spatial and temporal resolution.

Average velocities of some plasma species have been calculated from spatial and temporally resolved 2D OES images.

Electron density ($\sim 9\times10^{17}$ cm^{-3}) has been studied with spatial and temporal resolution.

Temporal evolution of the plasma temperature has been calculated by means of Boltzmann plots